Title: Abrupt cloud clearing of marine stratocumulus in the subtropical southeast Atlantic

Authors: Sandra E. Yuter[1*], John D. Hader[1,2], Matthew A. Miller[1], and David. B. Mechem[3]

Affiliations:

[1]Department of Marine, Earth, and Atmospheric Sciences, North Carolina State University, Raleigh, NC

[2]ICF, Fairfax, Virginia, USA

[3]Department of Geography and Atmospheric Science, University of Kansas, Lawrence, KS

*Correspondence to: seyuter@ncsu.edu

One sentence summary: Large areas of low clouds over the subtropical southeast Atlantic are rapidly removed by atmospheric disturbances 1000s of km long emanating from the African continent.

Abstract:
We document rapid and dramatic clearings of large portions of the subtropical marine low cloud deck that have implications for the global radiation balance and climate sensitivity. Over the southeast Atlantic, large areas of stratocumulus are rapidly eroded yielding partial or complete clearing along sharp transitions 100s to 1000s of km in length that move westward at 8-12 m s^{-1} and travel as far as 1000+ km from the African coast. The westward-moving cloudiness reductions have an annual peak in occurrence in April-May-June. The cloud erosion boundaries reduce cloud at ≈10 km scale in less than 15 min, move approximately perpendicular to the mean flow, and are often accompanied by small-scale wave features. Observations suggest that the cloud erosion is caused by atmospheric gravity waves.

Main Text:

The areal extent and temporal variability of subtropical marine low clouds strongly influence the global radiation balance (*1*). Large, persistent areas of subtropical marine stratocumulus clouds have been called the Earth's "climate refrigerator" (*2*). These low marine clouds scatter solar radiation back to space and emit thermal radiation at a temperature close to the sea surface temperature (SST), yielding net radiative cooling of the climate system. The controls on areal coverage of marine stratocumulus have historically been cast as either a steady-state response to an imposed large-scale mean forcing (e.g. SST, subsidence, inversion strength, radiative flux) (*3,4*) or dominated by internal aerosol–cloud–precipitation processes (*5-7*). Most previous work on low marine cloudiness transitions, including several studies addressing pockets of open cells, have predominantly employed frameworks that focus on responses to SST gradients and/or internal aerosol–cloud–precipitation processes and implicitly exclude external multi-day synoptic variability (*8,9*). Yet, a recent spectral analysis of multi-year global satellite data sets (*10*) found that cloudiness variance at multi-day (3-50 days) timescales exceeds the seasonal variance over the subtropical southeast Atlantic and northeast Pacific and is only slightly lower than the seasonal magnitude over the subtropical southeast Pacific. Abrupt

changes in regional albedo from 0.9 (mostly low cloud cover) to 0.6 (mostly ocean under clear sky) will substantially increase the shortwave radiation absorbed by the ocean, which has pronounced implications for marine ecology and biogeochemistry (*11*).

Cloudiness transition boundaries 100s to 1000s of km long in the southeast Atlantic exhibit abrupt reductions of cloud akin to pulling away a sun shade (Fig. 1, Movie S1, Movie S2, Movie S3, Movie S4). The information below is derived from 377 cloud erosion boundaries, identified from an examination of 1911 days over the period from 8 May 2012 through 31 July 2017 using MODIS corrected reflectance data and geosynchronous satellite visible and infrared data (see Methods for details). The cloud-eroding events in the southeast Atlantic occur year-round with a peak monthly frequency of occurrence of roughly 20 events per month in May (Fig. 2). The abrupt cloudiness transitions, up to 1000+ km in meridional length, move westward at 8-12 m s^{-1} from 11°E to as far as 4°W longitude, as much as 1500 km from the African coastline (Fig. 3). For any single cloudiness boundary, the speed of motion is relatively constant as the boundary moves westward (Fig. 3). At different locations along the same boundary, cloud reduction can result in partial or complete clearing (Fig. 1). Cloudiness transitions typically become discernible along the coast of southwestern Africa generally within a few hours of local midnight (Fig. 3, Movies S2 and S4). The removal of cloud at night indicates that short wave radiation-cloud feedbacks are not required. The prevailing winds at cloud level in this region are typically southerly or southeasterly (*12*), and individual features in the low cloud field can be tracked moving northward relative to the westward-moving cloud erosion boundary (Movie S1). The motion of the cloud erosion boundary is roughly perpendicular to the cloud-level winds and cannot be primarily explained by advection.

High resolution imagery of areas along the cloudiness boundaries often show a sharp and abrupt transition from overcast to clear or from overcast to broken cloud over spatial scales of ≤ 10 km (Fig. 1). Along some cloudiness boundaries, individual closed cells within the mesoscale cellular structure of the marine stratocumulus appear to be bisected (e.g. Fig. 1F and 1G). Animated loops of visible satellite imagery reveal that cloud cover over ≈10 km horizontal scales is removed or reduced in 15 minutes or less (Movies S1 and S3). Frequently occurring features near the cloud erosion boundaries are sets of wave-like, narrow (wavelength ≤ 10 km), elongated, banded features roughly parallel to the cloudiness boundary (Fig 1E and 1G).

Globally, satellite imagery reveals a rich array of multi-day marine low cloudiness variations, including sharp transitions between areas with nearly overcast and nearly clear conditions. Some of these cloudiness transition boundaries are associated with advection of low-level air from poleward extratropical cyclones into the subtropics (*13-15*). Cloud coverage, type, and height in the midlatitudes are clearly modulated by synoptic-scale baroclinic weather systems (*16-18*). Some subtropical cloudiness reductions are associated with inversion strength anomalies originating from higher-latitude synoptic storms (*10*). Aircraft measurements off the coast of California show that near-shore clearings of the marine cloud field can be associated with synoptic-scale perturbations in the alignment and strength of the northeast Pacific ridge and concurrent mesoscale circulations along the California coast (*19*). These near-shore clearings expand during the day and contract toward the coast at night.

Propagating atmospheric gravity waves (buoyancy oscillations) can manifest as transitions from overcast to broken cloud and from thicker to thinner clouds. A westward-moving diurnal atmospheric gravity wave originating over the heated, elevated terrain of the Andes modulates liquid water path (LWP) in marine low clouds over the southeast Pacific (*20-*

22). Intermittent atmospheric gravity wave trains originating from a disturbed subtropical jet can move equatorward into the southeast Pacific subtropical cloud deck, modulate LWP, and reduce cloud fraction during the day (*23, 24*).

The characteristics of the southeast Atlantic cloud clearings are inconsistent with advection and the specific gravity wave mechanisms documented in the southeast Pacific. The westward motion of the southeast Atlantic cloudiness transitions in an environment of prevailing southerly and southeasterly cloud-level winds, , and a persistent, large-scale stable layer topped by an inversion that can serve as a waveguide (*25*) strongly suggest that the cloud erosion is primarily caused by an atmospheric gravity wave rather than advection. Additionally, the combination of the direction of motion, phase speed, and timing characteristics of these wave-like phenomena over the subtropical southeast Atlantic differ from documented atmospheric gravity waves over the subtropical southeast Pacific. The westward-moving diurnal solitary wave over the southeast Pacific is associated with heating of elevated terrain and crosses the coast at about 1700 local time (*20,21*). This westward-propagating atmospheric gravity wave has a wavelength of ≈400 km, a phase speed of 30 m s^{-1}, and wave depth of 5 km. The northeastward-moving atmospheric gravity wave trains that emerge from a disturbed subtropical jet and propagate towards the coast of Peru (*23, 24*) have wavelengths of 50 to 100 km, a vertical displacement of ≈400 m, and a phase speed of ≈15 m s^{-1}. The wavelength and vertical displacement of the 1000+ km long southeast Atlantic cloud-eroding waves are currently not known, though the phase speed is in the range of 8-12 m s^{-1} and evidence of waves with wavelength ≤ 10 km can be observed concomitantly with the cloudiness transitions (Fig 1E and 1G).

Throughout the year in the southeast Atlantic, we also observed small-scale propagating cloud wave trains moving toward the south, southwest, southeast, and east. Figure 4 and Movies S5 and S6 show an example when overlapping cloud wave trains moved southeastward, southwestward, and eastward coincident with westward-moving cloud erosion. Cloud wave trains associated with deep convective latent heating were documented off the northwest coast of Australia during seasons when deep convection was common over the nearby continent (*26*). A potential source for southward-moving atmospheric gravity waves in the southeast Atlantic is latent heating from tropical deep convection (*27*) over western equatorial Africa and from the Atlantic Intertropical Convergence Zone. The eastward-moving wave trains in the southeast Atlantic may originate from the disturbed subtropical jet similar to cloudiness perturbations seen in the southeast Pacific (*23*).

Cloud generation by atmospheric gravity waves is extensively documented in the literature, and the associated physical mechanisms are reasonably well understood (*26, 28-32,* see Supplementary text for details). These studies show that when moisture and stability conditions are favorable, upward motions within the waves can yield propagating lines of clouds hundreds of km in length moving on the order of 10 m s^{-1}.

In contrast, cloud-eroding waves defy easy explanation. The upward and downward motion associated with atmospheric gravity wave passage should yield reversible changes. For a parcel with a given temperature and specific humidity, upward motion decreases the temperature, increases relative humidity, and if saturation occurs can yield cloud. Downward motion increases temperature and decreases relative humidity. If the moisture content of the air is unchanged, cloudiness would increase with upward motion, decrease with downward motion, and return to the pre-wave cloud state once the wave passes through. Yet observations show that cloud erodes

along the boundaries in an irreversible manner that yields reduced cloud fraction for hours (Movies S2 and S4).

For atmospheric gravity wave-induced cloud clearing to occur, a wave must be excited and then must propagate through a layer of the atmosphere that includes the top of the marine boundary layer where the clouds reside. Further, the wave needs to be associated with a localized mechanism that can irreversibly reduce cloud fraction on time scales of 10s of minutes. Lastly, the cloud deck itself must be susceptible to this erosion by the atmospheric gravity wave.

Why abrupt cloud clearing over the subtropical southeast Atlantic is most frequent in May is related to some combination of environmental conditions favoring the presence of the above factors in the region and season of interest compared to other seasons and regions. MODIS aerosol optical depth measurements show that abrupt cloudiness transitions occur in a variety of aerosol conditions (Fig. S1). Comparison of large-scale conditions derived from the MERRA reanalysis for May, the month with the most cloud erosion boundaries, and for January, the month with the fewest, indicates weaker stability in May compared to January (median estimated inversion strength of 4.3 K vs. 5.1 K) but stronger subsidence (700 hPa vertical pressure velocity of 0.049 Pa s^{-1} vs. 0.032 Pa s^{-1}).

Our hypothesis is that westward-moving atmospheric gravity waves cause the abrupt cloudiness transitions in the southeast Atlantic and are triggered by the interaction of offshore flow – likely combining a nocturnal land breeze and downslope winds from the coastal highlands (*33*) – with the stable marine boundary layer in a manner similar to processes that generate cloud-forming atmospheric gravity waves (*26, 28, 30,31*). For individual cloud erosion boundaries, we typically do not see evidence of slowing with increasing distance from the coast, as would be expected from a thinning, dissipating cold air mass originating over land (Fig. 3). Among the three subtropical marine stratocumulus cloud decks in the northeast Pacific, southeast Pacific, and southeast Atlantic, the southeast Atlantic has the largest diurnal wind variability near the adjacent coast (*34*), which would be consistent with regular offshore flow events triggering gravity waves. Comparable westward-moving dramatic cloud clearing events are not common in either the southeast Pacific or northeast Pacific.

The removal of cloud over 10s of minutes and the observation of bisected closed cellular cloud structures suggests a fast-acting mechanism. We hypothesize that cloud erosion is a consequence of rapid entrainment of warm and dry air from the free troposphere into the cloud layer by enhanced turbulence associated a solitary wave train excited by offshore flow emanating from southwest Africa. Locally-enhanced turbulent kinetic energy and mixing across the inversion has been documented within a solitary wave packet in the central United States (*35*).

Targeted observations in the subtropical southeast Atlantic including dropsondes and airborne radar and lidar measurements will be needed to resolve the mechanisms for rapid cloud erosion along cloud-eroding boundaries. The meteorological conditions associated with the formation and lack of formation of the cloudiness boundaries as well as features of downslope winds and their interactions with marine stable layer are currently being investigated using a combination of observations, reanalysis, and mesoscale modeling.

Persistent, wide-area reductions in cloud fraction over 100's of km scales associated with these westward-moving cloud erosion boundaries contribute to a lower March-April-May average cloud fraction in the subtropical southeast Atlantic compared to any season in the subtropical southeast Pacific or the subtropical northeast Pacific (*36*). Mechanisms that yield

substantial multi-day variability in marine stratocumulus cloud fraction are highly relevant to the climate system. Cloud-system resilience to external multi-day perturbations and the frequency of these perturbations may be key factors in governing low-cloud variability and potential climate sensitivity.

Supplementary Materials

Materials and Methods

Supplementary text

Table S1

Fig. S1

References (37-55)

Captions for Movies S1 to S6

Other Supplementary Materials for this manuscript includes the following:

Movies S1 to S6

References and Notes:

1. D. L. Hartmann, M. E. Ockert-Bell, M. L. Michelsen, The effect of cloud type on Earth's energy balance: Global analysis. *J. Climate* **5**, 1281–1304 (1992).
2. C. S. Bretherton, *et. al.*, The EPIC 2001 Stratocumulus Study. *Bull. Amer. Meteor. Soc.* **85**, 967–977 (2004).
3. W. H. Schubert, J. S. Wakefield, E. J. Steiner, S. K. Cox, Marine stratocumulus convection. Part I: Governing equations and horizontally homogeneous solutions. *J. Atmos. Sci.* **36**, 1286–1307 (1979).
4. B. Stevens, Entrainment in stratocumulus-topped mixed layers. *Q.J.R. Meteorol. Soc.* **128**, 2663–2690 (2002).
5. B. Stevens, W. R. Cotton, G. Feingold, C.-H. Moeng, Large-Eddy Simulations of strongly precipitating, shallow, stratocumulus-topped boundary layers. *J. Atmos. Sci.* **55**, 3616– 3638 (1998).
6. A. S. Ackerman, *et.al.*, Large-Eddy Simulations of a drizzling, stratocumulus-topped marine boundary layer. *Mon. Wea. Rev*. **137**, 1083–1110 (2009).
7. R. Wood, *et. al.*, An aircraft case study of the spatial transition from closed to open mesoscale cellular convection over the Southeast Pacific. *Atmos. Chem. Phys.* **11**, 2341–2370 (2011).
8. I. Sandu, B. Stevens, On the Factors Modulating the stratocumulus to cumulus transitions. *Journal of the Atmospheric Sciences* **68**, 1865–1881 (2011).
9. A. H. Berner, C. S. Bretherton, R. Wood, A. Muhlbauer, Marine boundary layer cloud regimes and POC formation in a CRM coupled to a bulk aerosol scheme. *Atmos. Chem. Phys.* **13**, 12549–12572 (2013).
10. S. P. de Szoeke, K. L. Verlinden, S. E. Yuter, D. B. Mechem, The time scales of variability of marine low clouds. *J. Climate* **29**, 6463–6481 (2016).
11. C. Brunet, R. Casotti, V. Vantrepotte, Phytoplankton diel and vertical variability in photobiological responses at a coastal station in the Mediterranean Sea. *Journal of Plankton Research* **30**, 645–654 (2008).
12. C. M. Risien, D. B. Chelton, A Global Climatology of Surface Wind and Wind Stress Fields from Eight Years of QuikSCAT Scatterometer Data. *J. Phys. Oceanogr.* **38**, 2379–2413 (2008).
13. S. A. Klein, Synoptic Variability of low-cloud properties and meteorological parameters in the subtropical trade wind boundary layer. *J. Climate* **10**, 2018–2039 (1997).
14. M. A. Rozendaal, W. B. Rossow, Characterizing some of the influences of the general circulation on subtropical marine boundary layer clouds. *J. Atmos. Sci.* **60**, 711–728 (2003).
15. R. C. George, R. Wood, Subseasonal variability of low cloud radiative properties over the southeast Pacific Ocean. *Atmos. Chem. Phys.* **10**, 4047–4063 (2010).
16. N.-C. Lau, M. W. Crane, A satellite view of the synoptic-scale organization of cloud properties in midlatitude and tropical circulation systems. *Mon. Wea. Rev.* **123**, 1984– 2006 (1995).
17. S. A. Klein, C. Jakob, Validation and sensitivities of frontal clouds simulated by the ECMWF model. *Mon. Wea. Rev.* **127**, 2514–2531 (1999).
18. G. L. Stephens, Cloud feedbacks in the climate system: A critical review. *J. Climate* **18**, 237–273 (2005).
19. E. Crosbie, *et al.*, Stratocumulus cloud clearings and notable thermodynamic and aerosol contrasts across the clear cloudy interface. *J. Atmos. Sci.* **73**, 1083–1099 (2015).

20. R. Garreaud, R. Muoz, The diurnal cycle in circulation and cloudiness over the subtropical southeast Pacific: A Modeling Study. *Journal of Climate* **17**, 1699–1710 (2004).
21. C. W. ODell, F. J. Wentz, R. Bennartz, Cloud liquid water path from satellite-based passive microwave observations: A new climatology over the global oceans. *J. Climate* **21**, 1721–1739 (2008).
22. R. Wood, M. Khler, R. Bennartz, C. O'Dell, The diurnal cycle of surface divergence over the global oceans. *Q.J.R. Meteorol. Soc.* **135**, 1484–1493 (2009).
23. G. Allen, *et al.*, Gravity-wave-induced perturbations in marine stratocumulus. *Q.J.R. Meteorol. Soc.* **139**, 32–45 (2013).
24. P. J. Connolly, *et al.,* Modelling the effects of gravity waves on stratocumulus clouds observed during VOCALS-UK. *Atmos. Chem. Phys.* **13**, 7133–7152 (2013).
25. S. A. Klein, D. L. Hartmann, The seasonal cycle of low stratiform clouds. *J. Climate* **6**, 1587–1606 (1993).
26. C. E. Birch, M. J. Reeder, Wave-cloud lines over northwest Australia. *Q.J.R. Meteorol. Soc.* **139**, 1311–1326 (2013).
27. B. E. Mapes, Gregarious Tropical Convection. *J. Atmos. Sci.* **50**, 2026–2037 (1993).
28. R. H. Clarke, R. K. Smith, D. G. Reid, The Morning Glory of the Gulf of Carpentaria: An atmospheric undular bore. *Mon. Wea. Rev.* **109**, 1726–1750 (1981).
29. D. R. Christie, K. J. Muirhead, R. H. Clarke, Solitary waves in the lower atmosphere. *Nature* **293**, 46–49 (1981).
30. F. Dsalmand, A. Szantai, L. Picon, M. Desbois, Systematic observation of westward propagating cloud bands over the Arabian Sea during Indian Ocean Experiment (INDOEX) from Meteosat-5 data. *J. Geophys. Res.* **108**, 8004 (2003).
31. J. C. B. da Silva, J. M. Magalhaes, Satellite observations of large atmospheric gravity waves in the Mozambique Channel. *Int. J. Remote Sens.* **30**, 1161–1182 (2009).
32. P.A. Lutzak, A proposal for analyzing and forecasting lower-atmospheric undular bores in the western Gulf of Mexico region. *Wea. Forecasting* **28**, 55–76 (2012).
33. T. Qian, C. C. Epifanio, F. Zhang, Topographic effects on the tropical land and sea breeze. *J. Atmos. Sci.* **69**, 130–149 (2012).
34. S. T. Gille, Global observations of the land breeze. *Geophys. Res. Lett.* **32,** (2005).
35. S. E. Koch, *et al.,* Turbulent mixing processes in atmospheric bores and solitary waves deduced from profiling systems and numerical simulation. *Mon. Wea. Rev.* **136**, 1373–1400 (2008).
36. C. D. Burleyson, S. E. Yuter, Subdiurnal stratocumulus cloud fraction variability and sensitivity to precipitation. *J. Climate* **28**, 2968–2985 (2015).
37. MODIS Web. http://modis.gsfc.nasa.gov/about/specifications.php
38. R. C. Levy, *et al.,* The Collection 6 MODIS aerosol products over land and ocean. *Atmos. Meas. Tech.* **6**, 2989–3034 (2013).
39. EOSDIS Worldview. https://worldview.earthdata.nasa.gov/
40. EUMSETSAT Product Navigator. http://navigator.eumetsat.int/
41. Globally-merged Full Resolution IR Brightness Temperature Data GES DISC - Goddard Earth Sciences Data and Information Services Center. https://disc.gsfc.nasa.gov/datasets/GPM_MERGIR_V1/summary?keywords=GPM_MERGIR_1
42. J. E. Janowiak, R. J. Joyce, Y. Yarosh, A real time global half hourly pixel resolution infrared dataset and its applications. *Bull. Amer. Meteor. Soc.* **82**, 205–217 (2001).

43. M. M. Rienecker, *et al.,* MERRA: NASA's Modern-Era Retrospective Analysis for research and applications. *J. Climate* **24**, 3624–3648 (2011).
44. J. Hader, Propagating, "Cloud-eroding Boundaries in Southeast Atlantic Marine Stratocumulus", North Carolina State University (2016).
45. J. M. Magalhaes, *et al.,* Atmospheric gravity waves in the Red Sea: A new hotspot. *Nonlin. Processes Geophys*. 18, 71–79 (2011).
46. R. H. Clarke, The Morning Glory: An atmospheric hydraulic jump. *J. Appl. Meteor*. **11**, 304–311 (1972).
47. D. R. Christie, The morning glory of the Gulf of Carpentaria: A paradigm for nonlinear waves in the lower atmosphere. *Aust. Meteorol. Mag.* **41**, 21–60 (1992).
48. R. K. Smith, G. Roff, N. Crook, The Morning Glory: An extraordinary atmospheric undular bore. *Q.J.R. Meteorol. Soc.* **108**, 937–956 (1982).
49. C. E. Birch, M. J. Reeder, G. J. Berry, Wave-cloud lines over the Arabian Sea. *J. Geophys. Res. Atmos.* **119**, 4447–4457 (2014).
50. T. A. Coleman, K. R. Knupp, Radiometer and profiler analysis of the effects of a bore and a solitary wave on the stability of the nocturnal boundary layer. *Mon. Wea. Rev.* **139**, 211–223 (2010).
51. V. C. Tsai, H. Kanamori, J. Artru, The morning glory wave of southern California. *J. Geophys. Res. Solid Earth* **109**, (2004).
52. D. R. Christie, K. J. Muirhead, A. L. Hales, On solitary waves in the atmosphere. *J. Atmos. Sci.* **35**, 805–825 (1978).
53. J. R. Holton, G. J. Hakim, *An Introduction to Dynamic Meteorology* (Elsevier, 2013).
54. A. A. Adebiyi, P. Zuidema, S. J. Abel, The convolution of dynamics and moisture with the presence of shortwave absorbing aerosols over the southeast Atlantic. *J. Climate* **28**, 1997–2024 (2014).
55. D. Painemal, S. Kato, P. Minnis, Boundary layer regulation in the southeast Atlantic cloud microphysics during the biomass burning season as seen by the A-train satellite constellation. *J. Geophys. Res. Atmos.* **119**, 11,288–11,302 (2014).

Acknowledgments:

M. Tai Bryant, Edward Siu Chan, Levi Lovell, Spencer Rhodes, Emma Scott, and Laura Tomkins helped to analyze satellite data. **Funding:** This work was supported by US Department of Energy grants: DE-SC0006701, DE-SC0006736 and DE-SC0016522 and National Science Foundation AGS grants: 1656237 and 1656314. **Author contributions:** All authors contributed to formulation of the conceptual model, analysis design, interpretation of the data, and critical revision of the article. Hader did the majority of data acquisition and processing with Miller aiding in these efforts. Yuter drafted the article based in part on J. Hader's thesis (44). **Competing interests:** None of the authors have competing interests.

Data and materials availability: Satellite data sets used in this study are archived and accessible at: https://worldview.earthdata.nasa.gov/, http://navigator.eumetsat.int/discovery/Start/DirectSearch/DetailResult.do?f(r0)=EO:EUM:DAT:MSG:HRSEVIRI, https://disc.gsfc.nasa.gov/datasets/GPM_MERGIR_V1/summary?keywords=GPM_MERGIR_1 Dates and times for the 377 southeast Atlantic westward-moving cloud erosion boundaries are accessible at Open Science Foundation DOI 10.17605/OSF.IO/KR4JS.

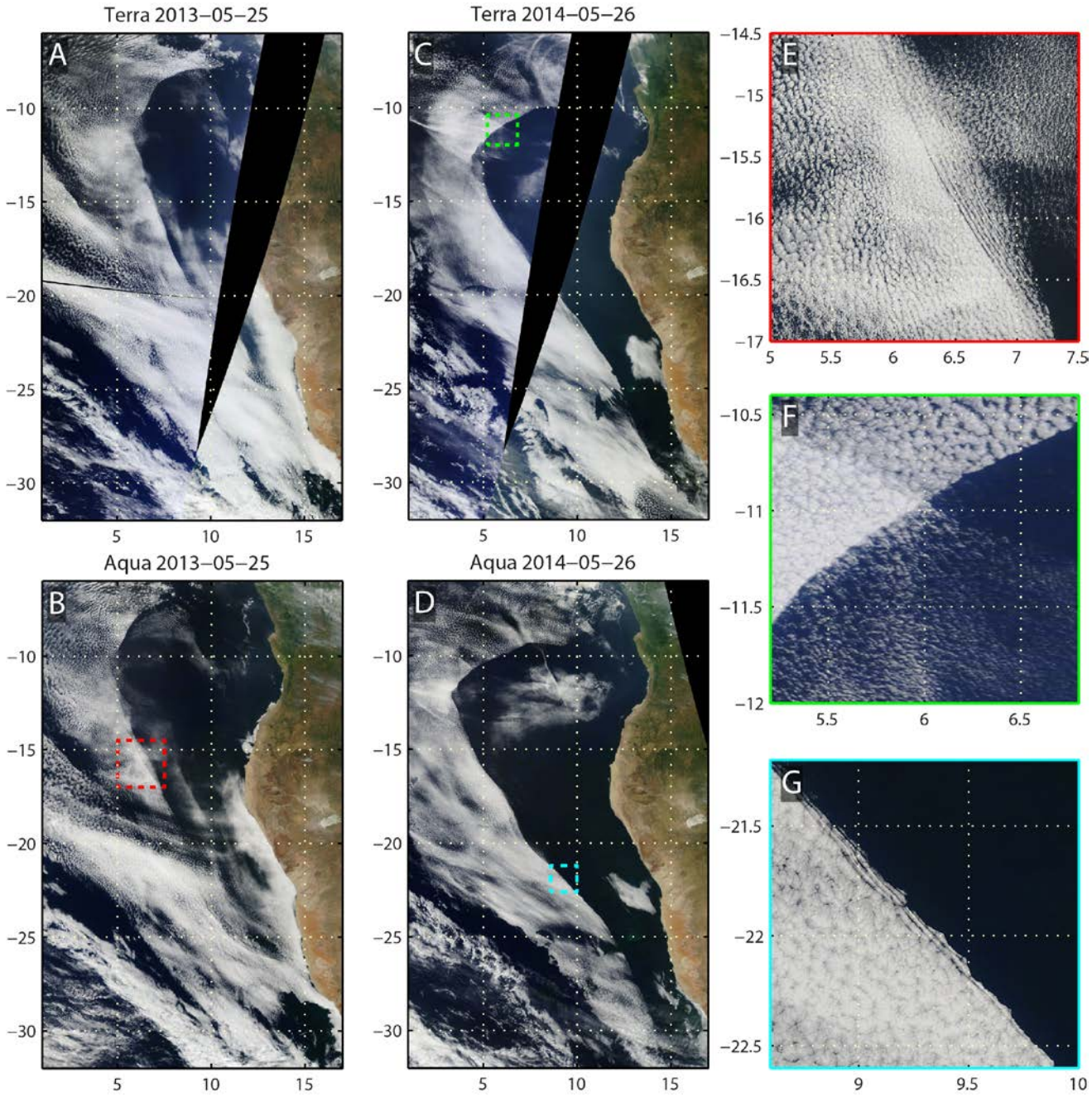

Fig. 1. Examples of westward-moving cloudiness transitions in the southeast Atlantic off the coast of Africa in MODIS corrected reflectance imagery. Consecutive pairs of Terra (≈1030am) and Aqua (≈1330pm) images (**A**), (**B**) on 25 May 2013 and (**C**), (**D**) on 26 May 2014. Detail inset (**E**) from panel (B), (**F**) from panel (C), and (**G**) from panel (D). Latitude and longitude grid shown with dashed lines. Movie loop animations of the 26 May 2014 case are shown in Movies S1 (reflectance) and S2 (IR).

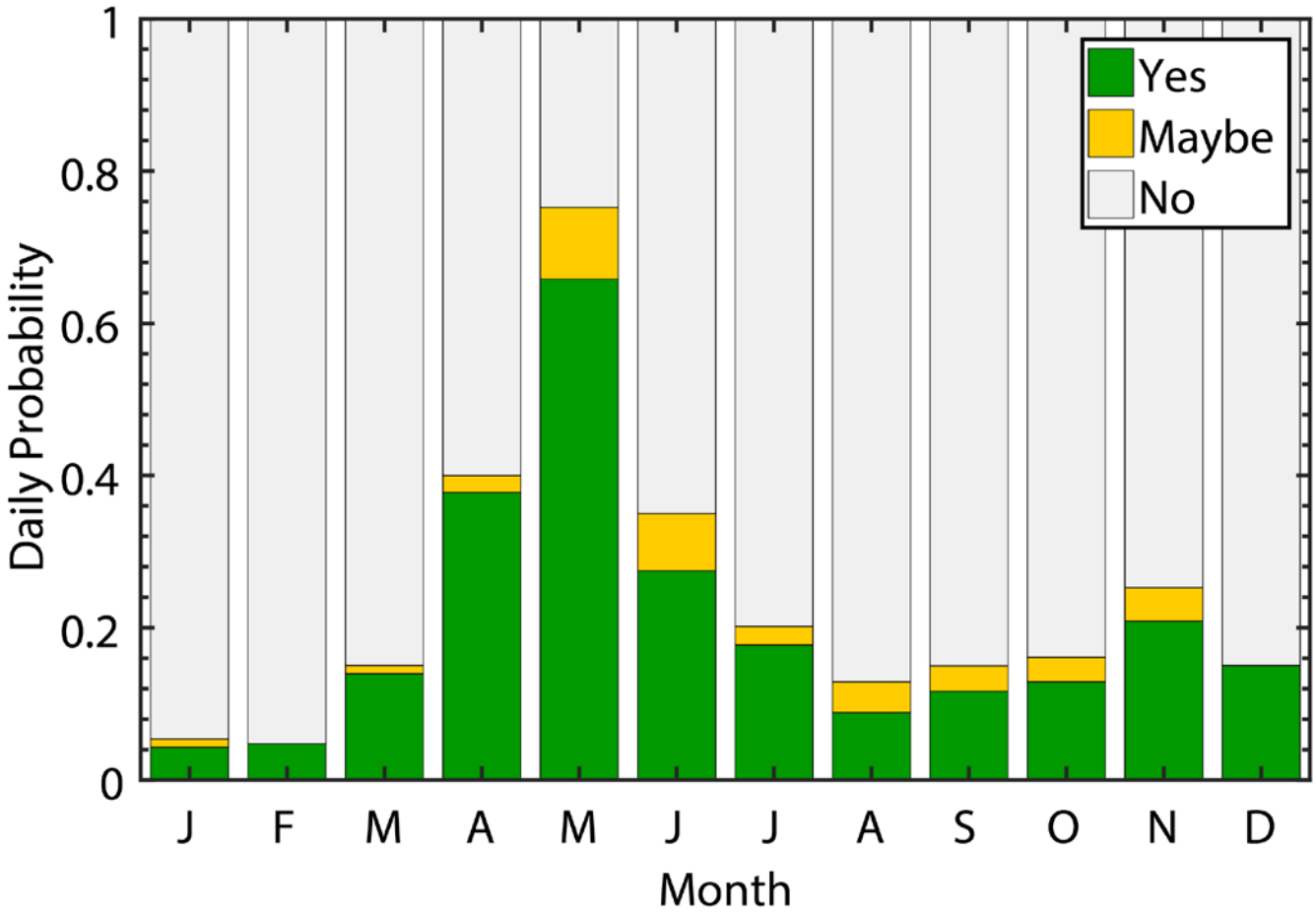

Fig. 2. Histogram of the daily probability of an abrupt cloudiness transition event occurring in a given month in the southeast Atlantic for the period 8 May 2012 through 31 July 2017. For example, the 0.658 daily probability value for the "Yes" events category for May means on average 20.4 of the 31 days of May have westward-moving cloud erosion boundaries over the southeast Atlantic. Analysis is based on pairs of Terra (morning) and Aqua (afternoon) visible corrected reflectance images. See Methods for details.

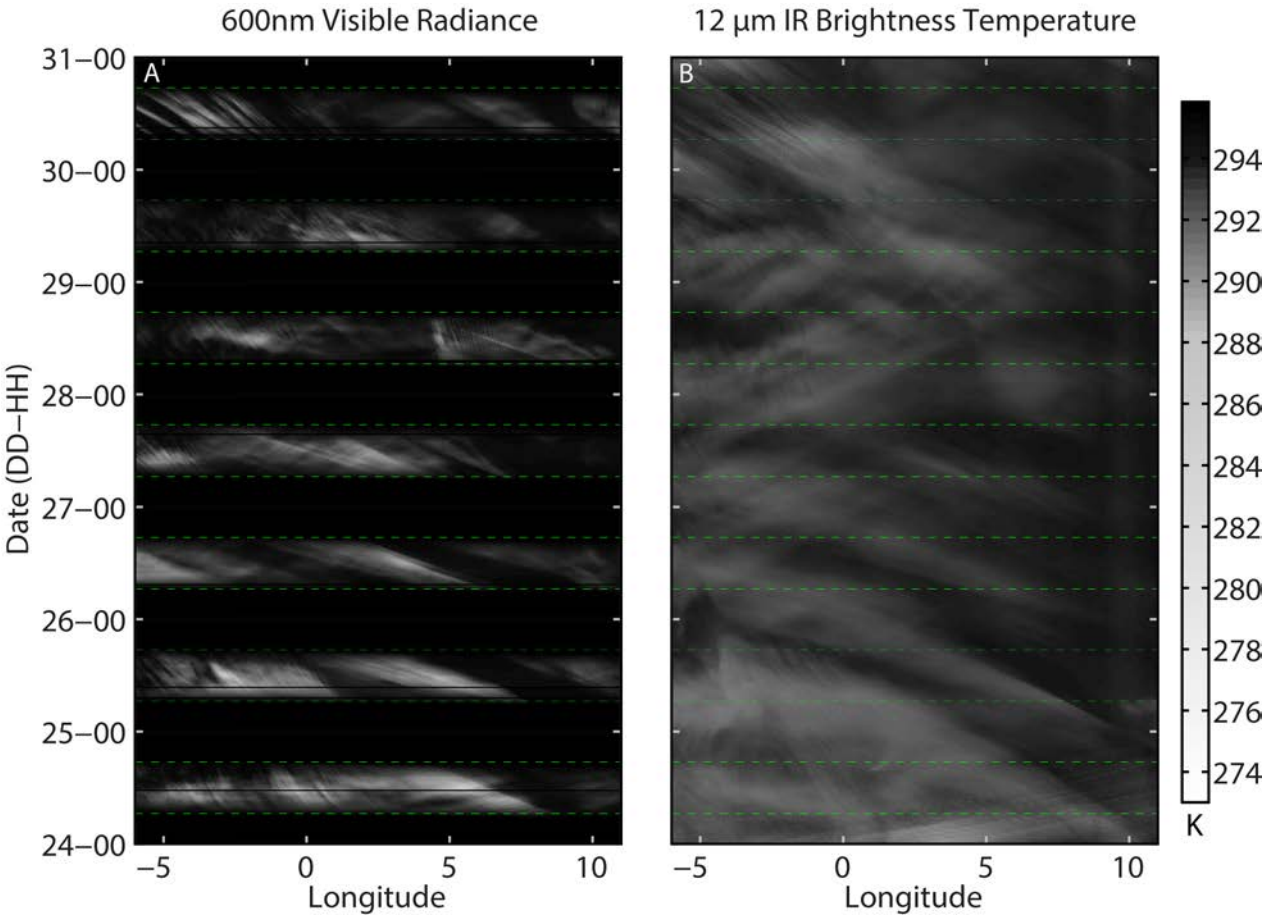

Fig. 3. Hovmöller plots illustrating cloud clearing event timing and propagation speed. (**A**) Meteosat 600 nm visible imagery and (**B**) 12 μm IR brightness temperature from 00 UTC 24 May 2014 to 00 UTC 31 May 2014. The dashed green lines denote the approximate sunrise and sunset times. Data are averaged meridionally over a box from 6°W to 11°E longitude and 12.5°S to 17.5°S latitude.

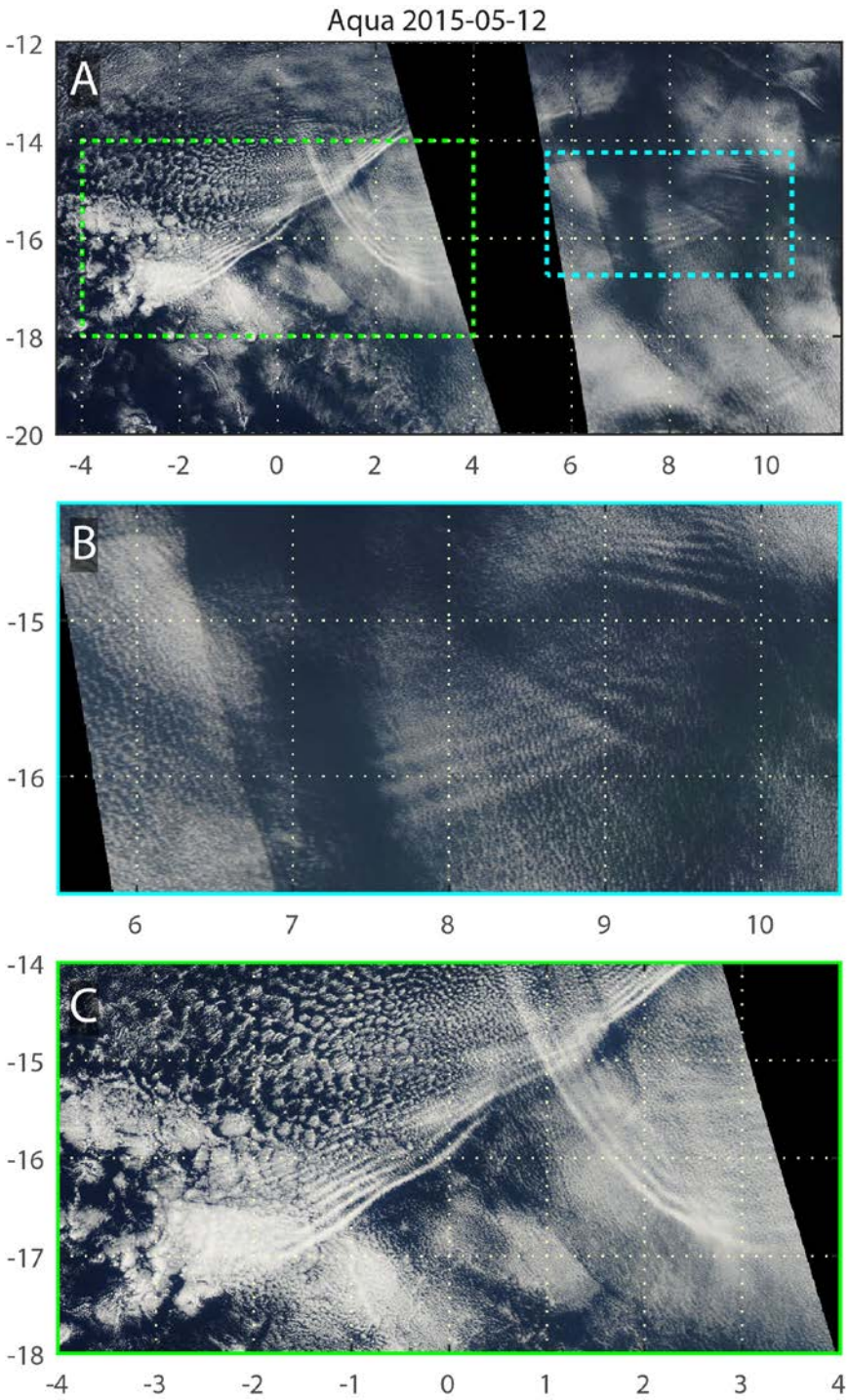

Fig. 4. Examples of multiple small-scale cloud wave trains propagating southeastward, southwestward, and eastward over the southeast Atlantic. MODIS corrected reflectance images centered off the west coast of Africa on 12 May 2015 during the afternoon Aqua overpass. (**A**) Regional image with 2° grid lines. (**B** and **C**) Close-ups of waves overlaid with 1° grid lines corresponding to the inset boxes denoted in (A). Movie loop animations of this case are shown in Movies S5 (reflectance) and S6 (IR).

Supplementary Materials for

Abrupt cloud clearing of marine stratocumulus in the subtropical southeast Atlantic

Sandra E. Yuter, John D. Hader, Matthew A. Miller, and David. B. Mechem

correspondence to: seyuter@ncsu.edu

This PDF file includes:

Other Supplementary Materials for this manuscript includes the following:

Movies S1 to S6

Materials and Methods

We use both polar-orbiting and geosynchronous satellite data in our analysis. A primary data set is the Moderate Resolution Imaging Spectroradiometer (MODIS) corrected reflectance true color data from the NASA Aqua and Terra satellites (*37*). We also examined MODIS Merged Dark Target/Deep Blue Aerosol Optical Depth (*38*) and Suomi-National Polar orbiting Partnership (Suomi-NPP) satellite Visible Infrared Imaging Radiometer Suite (VIIRS) corrected reflectance imagery. These data were obtained from NASA's Earth Observing System Data and Information System (EOSDIS) Worldview tool (*39*). The MODIS instrument has a swath width of 2330 km. The corrected reflectance data have an approximate pixel size of 250 m. The sun-synchronous orbits of the Terra and Aqua satellites result in data over the subtropical southeast Atlantic twice daily during daylight hours at roughly 10:30 LT (Terra) and 13:30 LT (Aqua) (MODIS). The Suomi-NPP satellite VIIRS corrected reflectance product is daylight only at roughly 13:30 LT and is provided at 250 meters resolution. The swath width is 3000 km. Along the southwestern African coast, the local time is one hour ahead of UTC, while the area further west near St. Helena Island (-15.9° latitude, -5.7° longitude), the local time aligns with UTC. For simplicity, we ignore the small discrepancy between UTC time and local time in the region of interest.

Short time-scale and short spatial-scale features of the marine stratocumulus erosion during daylight hours were examined using High Rate Spinning Enhanced Visible and IR Imager (SEVIRI) Level 1.5 visible satellite data from the Meteosat-10 geosynchronous satellite (centered at 0°latitude, 0°longitude). These data were obtained from the European Organization for the Exploitation of Meteorological Satellites (EUMETSAT) (*40*). Meteosat full-Earth scans are available roughly every 15 minutes with a pixel size between 3.1 and 4 km in the region of interest. Three-channel visible and near-infrared images using the 0.6 μm, 0.8 μm, and 1.6 μm channels were retrieved from the EUMETSAT Earth Observing Portal (*40*).

Half-hourly global merged infrared satellite data were obtained from NASA's Goddard Earth Sciences Data and Information Services Center (GES DISC) (*41)*. This merged infrared product is created by combining brightness temperature data from multiple geostationary satellites into a globally-complete brightness temperature data set on a uniform global grid with a pixel size of ≈4 km (*42*). The geosynchronous IR data are used to examine the brightness temperatures over the southeast Atlantic and southern Africa throughout the diurnal cycle.

Data from the Modern-Era Retrospective Analysis for Research and Application (MERRA) (*43*) were obtained through NASA's GES DISC. We used the 3-hourly instantaneous fields with a grid spacing of 0.5° latitude by 0.625° longitude, for the period 01 January 2000 through 31 December 2015. Monthly averages of 700 hPa pressure vertical velocity were computed from the daily-averaged meteorological variables to facilitate comparisons among different calendar months.

A sharp cloudiness transition boundary is defined as an abrupt transition (typically ≤10 km) between visually obvious regions of nearly overcast conditions to either decreased cloudiness or complete clearing (*44*). Our definition of a westward-moving cloudiness transition specifies that the boundary has to be at least 200 km in

length (≈2° latitude/longitude) and have a predominantly westward component of motion. In accordance with the latter criterion, most of the boundaries were oriented roughly in a north-south direction. We used visual examination of pairs of satellite images to tabulate days on which at least one westward-moving cloudiness transition occurred during the period from 8 May 2012 through 31 July 2017 in the region bounded by 10°S and 20°S latitude and 0° and 12°E longitude. Eight different analysts participated in examining the set of pairs of MODIS Aqua and Terra corrected reflectance images for each day (subsequently referred to as a 'cloud scene pair'). Each person was trained on the specific visual cues required to identify and categorize the boundaries and performed supervised practice on real examples before conducting the actual analysis. Most individuals analyzed 10-12 months of cloud scene pairs. To mitigate potential classification biases among individual analysts, cloud scene pairs for each day were analyzed by at least two people. The Terra and Aqua overpasses were analyzed in tandem to ascertain the movement of the boundary between the two overpasses (≈3 hours apart). When available, Suomi-NPP data were used to observe areas that fell in the gaps between Aqua MODIS swaths. The daily cloud scene pairs were categorized as definitely having a sharp cloudiness transition present ('yes'), definitely not having a sharp cloudiness transition present ('no'), or possibly having a sharp cloudiness transition present ('maybe'). In instances where the swath of the MODIS instrument missed a portion of the cloud deck, a 'yes', 'no', or 'maybe' decision was still made with the available information.

After this first round of cloud scene pair categorization, the two or more decisions for each cloud scene pair were compared. Scenes for which all analysts agreed on either a 'yes' or 'no' categorization were placed into the respective categories. For instances in which the analyzers disagreed or at least one analyzer indicated a 'maybe' categorization, the cloud scene pair was subsequently analyzed by two experienced satellite imagery analysts to determine if their categorization as 'yes', 'no', or 'maybe' could be resolved. For the 1911-day data set, there was a total of 377 'yes' days (days with a boundary present), 109 'maybe' days, and 1425 'no' days.

We consider the 'yes' subset of cloud scene pairs a robust underestimate of the actual number of cloudiness transitions that occur since it does not take into account multiple boundaries occurring on a single day or the 'maybe' category. Subjective analysis of satellite images to determine the occurrence frequency of atmospheric gravity waves has previously been done many times in the literature (*26, 28, 31, 45*).

A combination of Hovmöller diagrams based on Meteosat IR plus Aqua and Terra corrected reflectance image pairs were used to estimate the westward speed of the cloudiness transitions. We estimated speeds using several dozen pairs of Aqua and Terra images and about a dozen Hovmöller diagrams. Hovmöller diagrams of the satellite data were generated for the region between 6°W to 11°E longitude and 12.5°S to 17.5°S latitude (Fig. 3B). Brightness temperature values and corrected reflectance values within the analysis region were averaged meridionally for each 30-min and 15-min time step respectively.

Supplementary text

Propagating lines of clouds associated with atmospheric gravity waves occur in many locations throughout the world including the Morning Glory over the Gulf of Carpenteria (*28, 29, 46-48*), the northwest coast of Australia (*26*), the Mozambique Channel between Africa and Madagasar (*31*), the western Gulf of Mexico (*32*), and the Arabian Sea (*30,49*). Similar dynamics have been documented in gravity waves that do not produce lines of clouds over the Red Sea (*45*), in Alabama (*50*), and over the Los Angeles Basin (*51*). The wave-cloud lines are all associated with increases in boundary layer height from either single solitary waves, solitary wave packets, and/or bores. The interaction between a density current and a stable layer can generate a leading undular bore and a trailing set of solitary waves that together raise the height of the boundary layer for several hours (*32, 35*).

Data from microbaragraph and infrasonic arrays in northwest Australia illustrated that waves of elevation were much more common than those of depression in that region (*52*). Over a two-year period, 99 solitary waves of elevation were observed compared to only 3 'down-up' single solitary waves of depression (*52*). The waves of depression occurred in clear skies and from their phase speed characteristics were inferred to be high altitude rather than boundary layer structures.

The observed westward speed of motion of the cloud-eroding boundaries, as derived from the Hovmöller diagrams of IR and visible geosynchronous satellite data as well as the Terra and Aqua MODIS corrected reflectance overpasses, was found to be 8-12 ms^{-1}. To compare this observed speed to theory, we calculated the intrinsic gravity wave phase speed of the environment (*53*):

$$c = \frac{N}{\sqrt{(\frac{2\pi}{L_x})^2 + (\frac{2\pi}{L_z})^2}} \quad (1)$$

where N is the Brunt Väisälä frequency, and L_x and L_z are the horizontal and vertical wavelengths. Horizontal wavelengths of 2, 5, and 8 km are estimated based on observations of wave features along the cloud-eroding boundaries in Terra and Aqua MODIS corrected reflectance images. Given the dearth of operational upper sounding stations along the southwest African coasts of Nambia and Angola, we used upper air soundings from St. Helena Island, the nearest operational sounding station which is 1800 km from coast of Africa, (*54*) to estimate inversion height and Brunt Väisälä frequency characteristics. We used the subset of soundings from 2000 through 2011 that exhibited a strong inversion (i.e. a change in potential temperature of at least 8 K within a 300 m layer) and were obtained in an environment where the daily average lower tropospheric stability between -5.625° and -16° longitude (from MERRA reanalysis data) varied by 3 K or less (i.e., they were obtained in conditions where the environment at St. Helena Island was expected to be reasonably representative of the region adjacent to the African coast). This analysis yielded estimated maximum and minimum values of the Brunt Väisälä frequency of 0.052 s^{-1} and 0.04 s^{-1}. We used 1.75 km, the median inversion height from St. Helena Island in January as an estimated upper bound, and 1 km, the cloud top heights observed adjacent to the African coast during austral spring (*55*) as an estimated lower bound for the vertical wavelengths. The resulting intrinsic gravity wave phase speeds for the combinations of these parameters range from 5.7 to 14.1 ms^{-1} (Table S1)

Table S1: Intrinsic gravity wave phase speeds for various parameter values (in ms^{-1}). L_x denotes horizontal wavelength, L_z denotes vertical wavelength, and N denotes Brunt Väisälä frequency.

L_X (km)	N = 0.04 s^{-1} L_Z = 1 km	N = 0.04 s^{-1} L_Z = 1.75 km	N = 0.052 s^{-1} L_Z = 1 km	N = 0.052 s^{-1} L_Z = 1.75 km
2	5.7	8.4	7.4	10.9
5	6.2	10.5	8.1	13.7
8	6.3	10.9	8.2	14.1

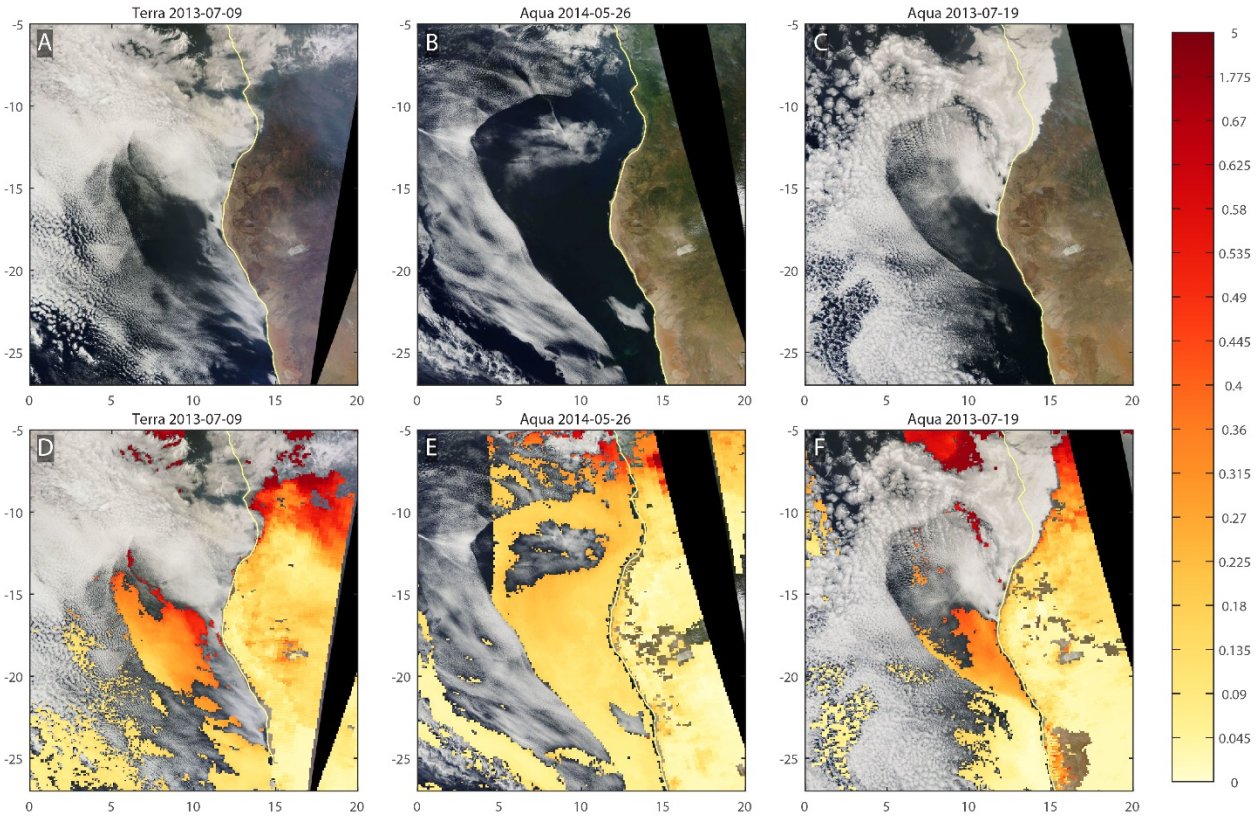

Fig. S1: Examples of cloud clearing events with corresponding aerosol optical depth estimates. MODIS Corrected Reflectance images for abrupt cloudiness transition events over the southeast Atlantic from (A) Terra on 9 July 2013, (B) Aqua on 26 May 2014, and (C) Aqua on 19 July 2013. (D, E, and F) The corresponding MODIS Merged Dark Target/Deep Blue Aerosol Optical Depth data overlaid on the MODIS Corrected Reflectance images.

References

37. MODIS Web. http://modis.gsfc.nasa.gov/about/specifications.php
38. R. C. Levy, *et al.,* The Collection 6 MODIS aerosol products over land and ocean. *Atmos. Meas. Tech.* **6**, 2989–3034 (2013).
39. EOSDIS Worldview. https://worldview.earthdata.nasa.gov/
40. EUMSETSAT Product Navigator. http://navigator.eumetsat.int/
41. Globally-merged Full Resolution IR Brightness Temperature Data GES DISC - Goddard Earth Sciences Data and Information Services Center. https://disc.gsfc.nasa.gov/datasets/GPM_MERGIR_V1/summary?keywords=GPM_MERGIR_1
42. J. E. Janowiak, R. J. Joyce, Y. Yarosh, A real time global half hourly pixel resolution infrared dataset and its applications. *Bull. Amer. Meteor. Soc.* **82**, 205–217 (2001).
43. M. M. Rienecker, *et al.,* MERRA: NASA's Modern-Era Retrospective Analysis for research and applications. *J. Climate* **24**, 3624–3648 (2011).
44. J. Hader, Propagating, "Cloud-eroding Boundaries in Southeast Atlantic Marine Stratocumulus", North Carolina State University (2016).
45. J. M. Magalhaes, *et al.,* Atmospheric gravity waves in the Red Sea: A new hotspot. *Nonlin. Processes Geophys*. 18, 71–79 (2011).
46. R. H. Clarke, The Morning Glory: An atmospheric hydraulic jump. *J. Appl. Meteor*. **11**, 304–311 (1972).
47. D. R. Christie, The morning glory of the Gulf of Carpentaria: A paradigm for nonlinear waves in the lower atmosphere. *Aust. Meteorol. Mag.* **41**, 21–60 (1992).
48. R. K. Smith, G. Roff, N. Crook, The Morning Glory: An extraordinary atmospheric undular bore. *Q.J.R. Meteorol. Soc.* **108**, 937–956 (1982).
49. C. E. Birch, M. J. Reeder, G. J. Berry, Wave-cloud lines over the Arabian Sea. *J. Geophys. Res. Atmos.* **119**, 4447–4457 (2014).
50. T. A. Coleman, K. R. Knupp, Radiometer and profiler analysis of the effects of a bore and a solitary wave on the stability of the nocturnal boundary layer. *Mon. Wea. Rev.* **139**, 211–223 (2010).
51. V. C. Tsai, H. Kanamori, J. Artru, The morning glory wave of southern California. *J. Geophys. Res. Solid Earth* **109**, (2004).
52. D. R. Christie, K. J. Muirhead, A. L. Hales, On solitary waves in the atmosphere. *J. Atmos. Sci.* **35**, 805–825 (1978).
53. J. R. Holton, G. J. Hakim, *An Introduction to Dynamic Meteorology* (Elsevier, 2013).
54. A. A. Adebiyi, P. Zuidema, S. J. Abel, The convolution of dynamics and moisture with the presence of shortwave absorbing aerosols over the southeast Atlantic. *J. Climate* **28**, 1997–2024 (2014).
55. D. Painemal, S. Kato, P. Minnis, Boundary layer regulation in the southeast Atlantic cloud microphysics during the biomass burning season as seen by the A-train satellite constellation. *J. Geophys. Res. Atmos.* **119**, 11,288–11,302 (2014).

Movie S1: Movie of 15-minute Meteosat visible imagery for 26 May 2014 from 05:00 to 18:15 UTC showing (left) regional view off the southwest coast of Africa and (right) close-up view corresponding to the yellow box on the left.

Movie S2: Movie of 30-minute merged infrared 12 μm brightness temperatures for the period from 25 May 2014 00:00 UTC to 27 May 2014 23:30 UTC showing a regional view of southern Africa and the southeast Atlantic. Red denotes missing data.

Movie S3: Movie of 15-minute Meteosat visible imagery for 26 May 2012 from 05:00 to 17:15 UTC showing (left) regional view off the southwest coast of Africa and (right) close-up view corresponding to the yellow box on the left.

Movie S4: Movie of 30-minute merged infrared 12 μm brightness temperatures for the period from 25 May 2012 00:00 UTC to 27 May 2012 23:30 UTC showing a regional view of southern Africa and the southeast Atlantic. Red denotes missing data.

Movie S5: Movie of 15-minute Meteosat visible imagery for 12 May 2015 from 05:00 to 17:45 UTC showing (left) regional view off the southwest coast of Africa and (right) close-up view corresponding to the yellow box on the left.

Movie S6: Movie of 30-minute merged infrared 12 μm brightness temperatures for the period from 11 May 2015 00:00 UTC to 13 May 2015 23:30 UTC showing regional view of southern Africa and the southeast Atlantic. Red denotes missing data.